Downloaded via SHREENIVAS DESHPANDE LIBRARY IIT (BHU) VARANASI on April 8, 2024 at 07:28:50 (UTC).
See https://pubs.acs.org/sharingguidelines for options on how to legitimately share published articles.

ACS OMEGA

Open Access
This article is licensed under CC-BY-NC-ND 4.0

http://pubs.acs.org/journal/acsodf
Article

Delineating the Structure−Dynamics−Binding Differences among BA.1, BA.4/5, and BF.7 SARS-CoV-2 Variants through Atomistic Simulations: Correlation with Structural and Epidemiological Features

Aryaman Joshi, Shweata Maurya, Atharva Mahale, Soumya Lipsa Rath, Timir Tripathi,* and Aditya K. Padhi*

Cite This: *ACS Omega* 2023, 8, 37852−37863

Read Online

ACCESS | Metrics & More | Article Recommendations | Supporting Information

ABSTRACT: Severe acute respiratory syndrome coronavirus 2 (SARS-CoV-2) is an RNA virus possessing a spike (S) protein that facilitates the entry of the virus into human cells. The emergence of highly transmissible and fit SARS-CoV-2 variants has been driven by the positive selection of mutations within the S-protein. Notable among these variants are alpha, beta, gamma, delta, and omicron (BA.1), with the latter contributing to significant global health challenges and impacting populations worldwide. Recently, a novel subvariant of BA.1, named BF.7, has surfaced, purportedly exhibiting elevated transmissibility and infectivity rates. In order to comprehend and compare the transmissibility and disease progression characteristics of distinct SARS-CoV-2 variants, we performed an extensive comparative analysis utilizing all-atom molecular dynamics (MD) simulations (in triplicate) to investigate the structural, dynamic, and binding features of BA.1, BA.4/5, and BF.7. Our simulation findings, energetic analysis, and assessment of physicochemical properties collectively illuminate the dominance of the BA.1 variant over the others, a trend that is further substantiated by the sustained global prevalence of BA.1 relative to BA.4/5 and BF.7. Additionally, our simulation results align well with the reported cryoelectron microscopy (cryo-EM) structural data and epidemiological characteristics obtained from the Global Initiative on Sharing All Influenza Data (GISAID). This study presents a comprehensive comparative elucidation of the critical structural, dynamic, and binding attributes of these variants, providing insights into the predominance of BA.1 and its propensity to continuously generate numerous novel subvariants.

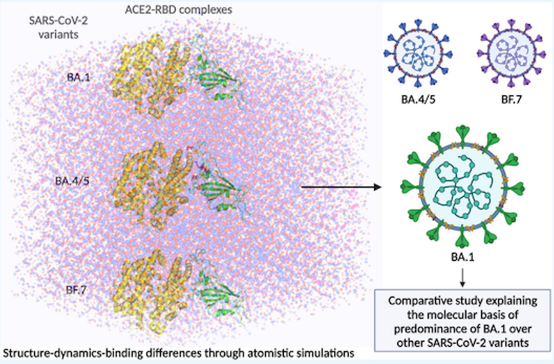

1. INTRODUCTION

Approximately four years into the COVID-19 pandemic and nearly three years since public access to vaccines commenced, we are continually struggling to neutralize the global threat due to the emergence of new variants. Since the roll of several vaccines, the disease has become no more than an occasional inconvenience for many people, but for others, the variants have proven deadly. The continuous emergence of new variants of severe acute respiratory syndrome coronavirus 2 (SARS-CoV-2) can be mainly attributed to its error-prone RNA polymerase machinery, immune and drug pressure,[1] and its genome, which encodes four main structural proteins, including spike (S), envelope (E), membrane (M), and nucleocapsid (N).[2,3] Among these, the S-protein is of particular significance because it has been shown to bind with the human angiotensin-converting enzyme 2 (ACE2) receptor through its receptor-binding domain (RBD). It has been reported that the rate of mutation in SARS-CoV-2 is estimated at two mutations per month[4] and at present, compared to the original strain, there are approximately 15 mutations in the BA.1, which vary from residue 333 to 527 in RBD.[1,5,6] These mutations can affect the transmissibility and infectivity rate, as they are part of the ACE2 and antibody-binding sites.[4,7,8]

The emergence of new mutations in SARS-CoV-2 can change their genetic makeup, making them more transmissible, virulent, or drug-resistant.[9−11] Additionally, new subvariants may also impact the efficacy of vaccines, making them less effective in preventing infection. According to the World Health Organization (WHO), SARS-CoV-2 variants are classified into a variant of concern (VOC) and variant of

Received: April 27, 2023
Accepted: September 7, 2023
Published: October 3, 2023

© 2023 The Authors. Published by American Chemical Society

https://doi.org/10.1021/acsomega.3c02904

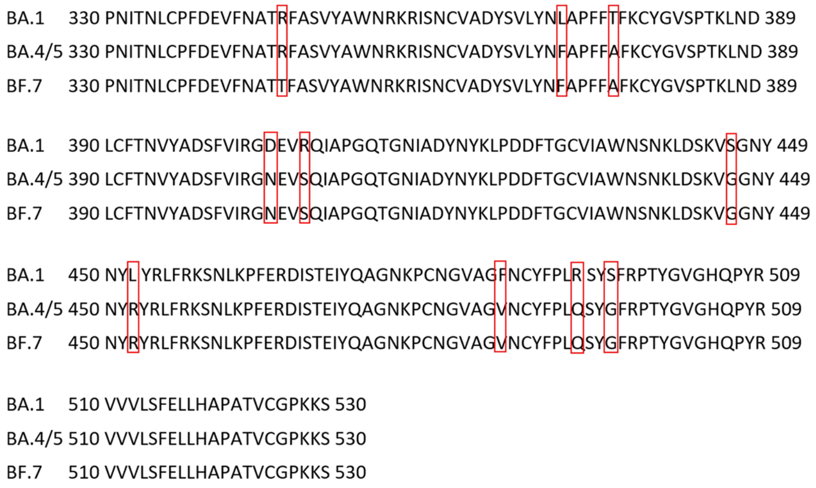

```
BA.1    330 PNITNLCPFDEVFNATRFASVYAWNRKRISNCVADYSVLYNLAPFFTFKCYGVSPTKLND 389
BA.4/5 330 PNITNLCPFDEVFNATRFASVYAWNRKRISNCVADYSVLYNFAPFFAFKCYGVSPTKLND 389
BF.7    330 PNITNLCPFDEVFNATTFASVYAWNRKRISNCVADYSVLYNFAPFFAFKCYGVSPTKLND 389

BA.1    390 LCFTNVYADSFVIRGDEVRQIAPGQTGNIADYNYKLPDDFTGCVIAWNSNKLDSKVSGNY 449
BA.4/5 390 LCFTNVYADSFVIRGNEVSQIAPGQTGNIADYNYKLPDDFTGCVIAWNSNKLDSKVGGNY 449
BF.7    390 LCFTNVYADSFVIRGNEVSQIAPGQTGNIADYNYKLPDDFTGCVIAWNSNKLDSKVGGNY 449

BA.1    450 NYLYRLFRKSNLKPFERDISTEIYQAGNKPCNGVAGFNCYFPLRSYSFRPTYGVGHQPYR 509
BA.4/5 450 NYRYRLFRKSNLKPFERDISTEIYQAGNKPCNGVAGVNCYFPLQSYGFRPTYGVGHQPYR 509
BF.7    450 NYRYRLFRKSNLKPFERDISTEIYQAGNKPCNGVAGVNCYFPLQSYGFRPTYGVGHQPYR 509

BA.1    510 VVVLSFELLHAPATVCGPKKS 530
BA.4/5 510 VVVLSFELLHAPATVCGPKKS 530
BF.7    510 VVVLSFELLHAPATVCGPKKS 530
```

Figure 1. Sequence alignment of the receptor-binding domain (RBD) among different SARS-CoV-2 variants (BA.1, BA.4/5, and BF.7) investigated in the study. Mutated residues across the sequence alignment of the three variants are highlighted by red boxes.

interest (VOI). Several subvariants have been identified, with 310 different lineages associated with them.[12] The "standard" sublineage is referred to as BA.1, while other sublineages include BA.2, BA.3, BA.4, and BA.5.[13] These sublineages share common mutations, but they also have significant differences.[14] BA.1 is the first dominant SARS-COV-2 variant that harbors 35 mutations in its S-protein from the original Wuhan strain.[15] BA.1 drove a large wave of infections and coronavirus disease and caused a strong immune escape from two mRNA vaccine dose-induced immunity.[7,9,16−19] Gradually, the BA.2 subvariant took over BA.1 because of its high transmissibility rate and immune evasion properties,[7] and further, BA.2 gave rise to several subvariants in quick successions. These included BA.4 and BA.5 subvariants, which had identical S-proteins and are referred to as BA.4/5. Notably, these subvariants rose to dominance and exhibited further immune escape.[7] The BA.4/5 has been identified as the driving variant, leading to further diversification with the emergence of several additional subvariants, including BA.4.6, BF.7, BQ.1 (derived from BA.4/5), and BA.2.75.2 (derived from BA.2.75).[7] Recently, a new variant, BF.7 (or BA.5.2.1.7), a sublineage of BA.5, has been identified as a variant of concern (VOC), with higher infectivity and transmissibility rates and a shorter incubation period among the other subvariants. It is assumed that the basic reproduction number (R0) of BF.7 is reportedly 10 to 18.6, while the average R0 of omicron is 5.08.

In this study, we performed a comparative analysis of the structural, dynamic, and binding characteristics of BA.1, BA.4/5, and BF.7 to correlate with experimental results and comprehend their transmissibility and disease progression. For this, the BA.1 crystal structure of RBD in complex with ACE2 was taken as a reference, and the structures of the complexes for BA.4/5 and BF.7 were modeled by incorporating the necessary mutations. Our study employing molecular modeling, MD simulations,[20] end-state binding free energy calculations, and related structural−dynamic analyses not only identifies several key features that result in the varied binding, activity, and interactions of the variants but also provides an explanation as to why BA.1 is still an aberrant variant of high significance with fitness advantages, transmissibility, and ability to generate numerous subvariants of unknown clinical and disease presentation.

2. MATERIALS AND METHODS

2.1. System Preparation. The crystal structure of the SARS-CoV-2 BA.1 S-protein RBD in complex with ACE2 was obtained from the Protein Data Bank (PDB ID: 7T9L). This was considered the wild-type structure, upon which several mutations were introduced to obtain BA.4/5 and BF.7. The mutagenesis function of PyMOL was used to model the mutations in BA.4/5 and BF.7.[7,21] From BA.1, six mutations (L371F, T376A, D405N, R408S, S446G, and S496G) were introduced to obtain BA.2, which was further subjected to the incorporation of three mutations (L452R, F486V, and R493Q). Finally, the R346T mutation was incorporated to obtain BF.7. Eventually, the quality of the prepared models was validated using the ERRAT[22] and PROCHECK[23,24] modules of the SAVES v6.0 server. Figure 1 represents the complete sequence alignment of the three variants, in which the mutated residues are highlighted in red.

2.2. Molecular Dynamics Simulations. These three systems (BA.1, BA.4/5, and BF.7) were subjected to all-atom MD simulations using the GROMACS 2022 package[25] along with the CHARMM36 force field.[26] The systems were solvated using the three-point TIP3P water model (for an explicit solvent model) in a cubic box with ∼20 Å between the protein surface and the box boundary. The addition of Na+ counterions subsequently neutralized each system. Each system was subjected to energy minimization for a maximum of 50,000 steps of the steepest descent algorithm until no energy fluctuation was observed. The systems were then heated by using a canonical ensemble that included heating from 0 to 300 K at 100 ps and an isobaric−isothermal ensemble that induced heating at 300 K for 100 ps. Following this, the systems were subjected to 100 ns production runs in NPT settings with a Berendsen thermostat[27] and a Parrinello−Rahman barostat.[28] For all simulations, the Fourier grid spacing and Coulomb radius were chosen to be 0.16 and 1.2 nm, respectively. The LINCS algorithm and particle mesh Ewald method were employed to calculate the long-range electrostatic forces.[29,30] The short-range van der Waals interactions were limited to 1.2 nm. For energy stabilization, root-mean-square deviation (RMSD) analysis, and monitoring convergence, snapshots were taken every 10 ps. To ensure the reproducibility and accuracy of the MD simulation results, we

Table 1. Systems Studied and the Corresponding Simulation Durations

si. no	system under study	simulation time (in triplicates)
1	BA.1	100 ns × 3
2	BA.4/5	100 ns × 3
3	BF.7	100 ns × 3

performed the all-atom MD simulations of all of the variants in triplicates.

2.3. Trajectory Analysis. The GROMACS utilities gmx rms, gmx rmsf, and gmx gyrate were used for the calculation of the root-mean-square deviation (RMSD), root-mean-square fluctuations (RMSF), and radius of gyration (R_g), respectively. Principal component analysis (PCA) was used to understand the dominant and collective modes of the RBD-ACE2 complex of distinct variants. The eigenvectors and eigenvalues and their projection along the first two principal components were derived using essential dynamics by constructing a variance/covariance matrix. For this purpose, the gmx covar and gmx anaeig modules were used to obtain the eigenvalues and eigenvectors. Further, the free energy landscape (FEL) of the RBD-ACE2 complex of the variations was highlighted using the gmx sham module, and three-dimensional (3D) contour plots of these FELs were produced using the corresponding principal components.

2.4. Binding Free Energy of the Variants. The binding free energy of the complex as well as between RBD and ACE2 for the three variants was calculated using gmx_MMPBSA.[31] It is a tool used to execute end-state free energy calculations, where the form of energy function used to calculate the potential energy of a molecular structure is referred to as molecular mechanics (MM), and the solvation term is expressed as the sum of polar and nonpolar elements. The detailed working principle and workflow of gmx_MMPBSA to perform such calculations are reported elsewhere.[1,32] For our analysis, Miniconda and Python3 were installed on the computing workstation. A fresh conda environment and all dependencies were subsequently installed to begin employing gmx_MMPBSA. The MMPBSA python script, the trajectory file, the topology file, and the index file containing RBD and ACE2 as two independent groups were utilized for executing gmx_MMPBSA. In addition, the gromacs portable topology files (.itp), protein structure file (.pdb or .psf), trajectory file (.xtc), protein topology file (.gro), and gromacs run topology files (.tpr) for both proteins were used as input. The final

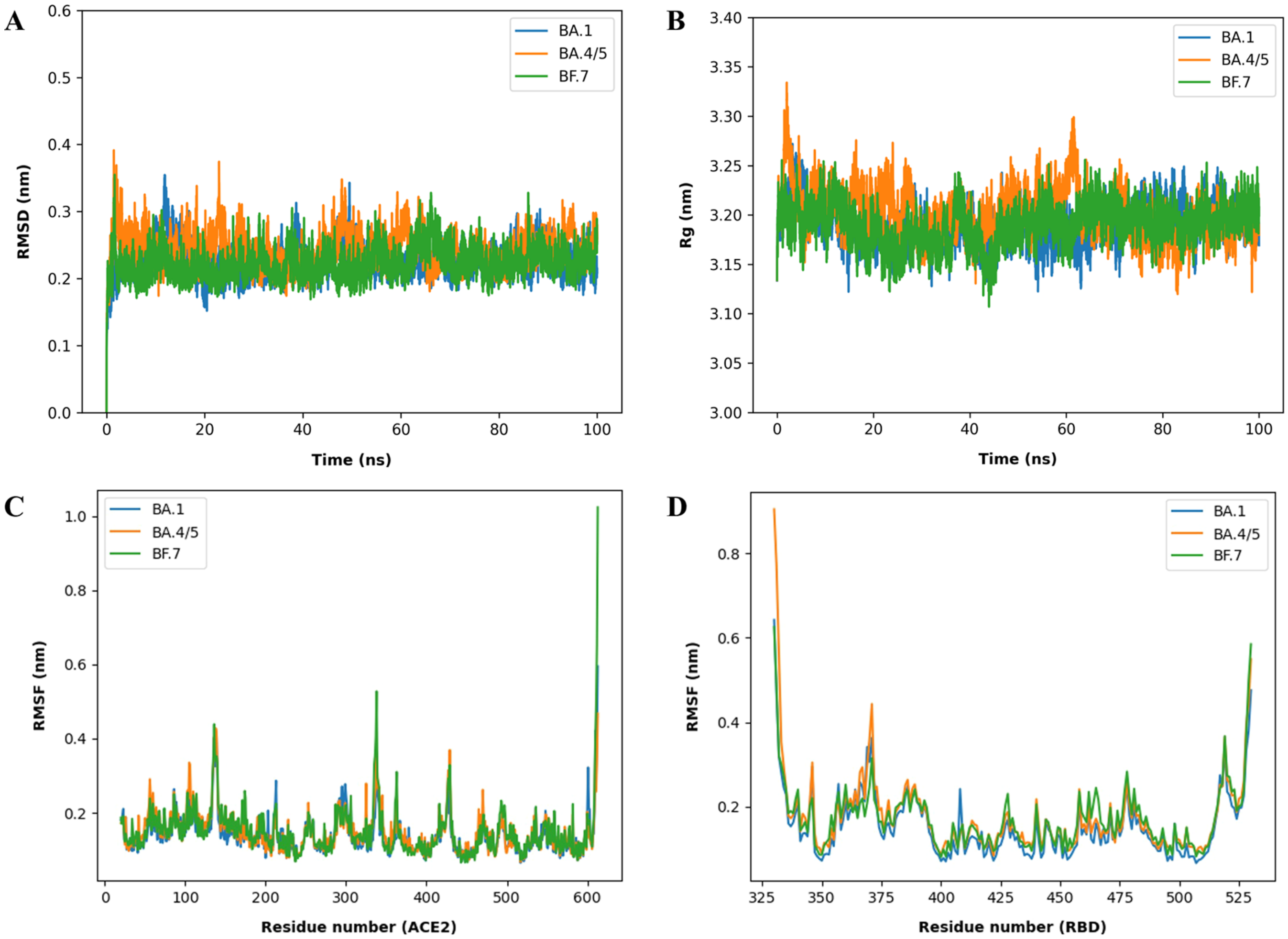

Figure 2. Comparative analysis of structural dynamics among BA.1, BA.4/5, and BF.7 variants of the RBD-ACE2 complex. (A) Root-mean-square deviation (RMSD) of the backbone atoms, (B) radius of gyration (R_g) of the RBD-ACE2 complex, (C) root-mean-square fluctuation (RMSF) of ACE2 residues, and (D) RMSF of RBD residues calculated over the entire 100 ns molecular dynamics (MD) simulations. The BA.1 variant exhibits greater stability, compactness, and reduced inherent flexibility compared to the other variants throughout the trajectory.

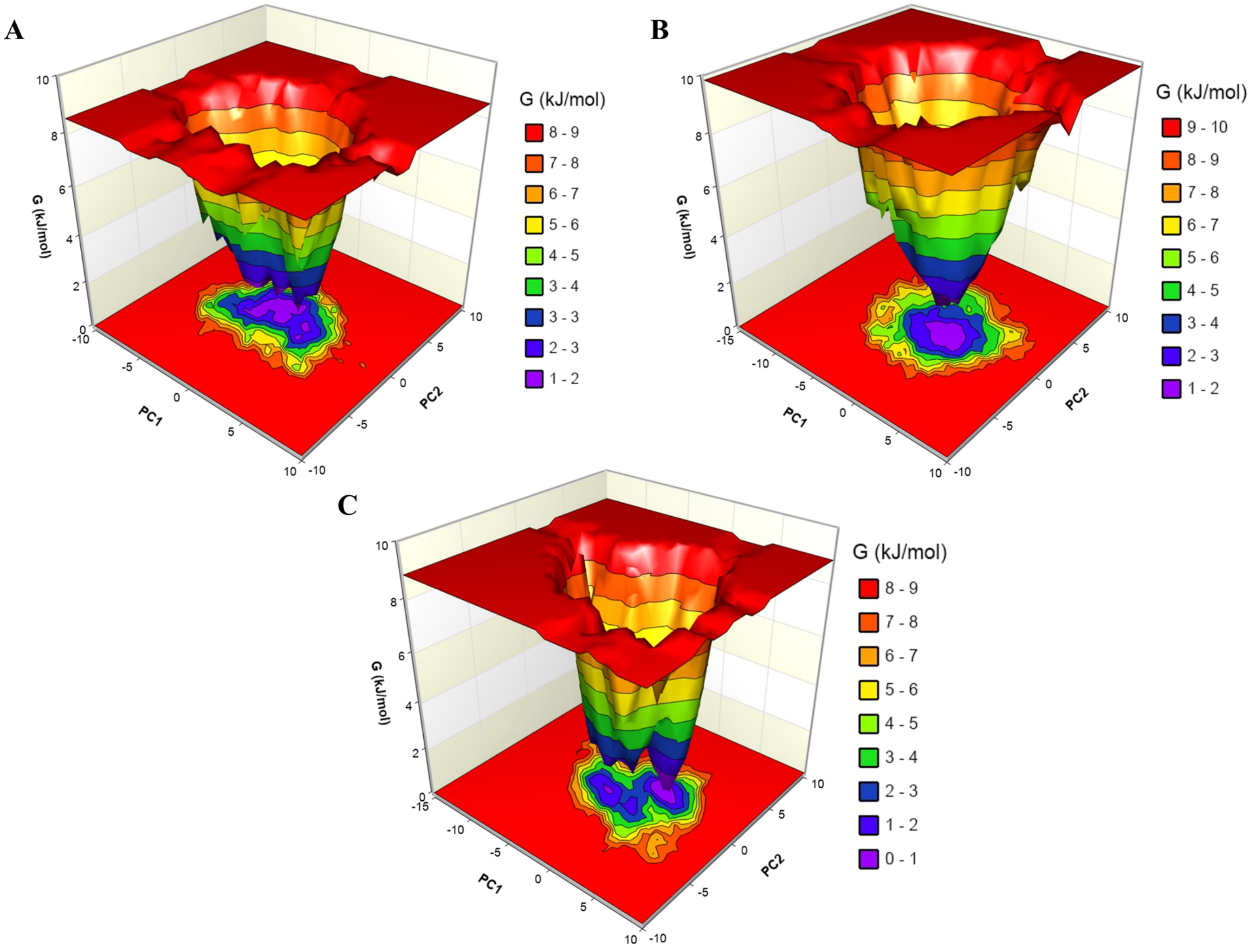

Figure 3. Gibbs free energy landscapes (FELs) of RBD-ACE2 complexes for BA.1, BA.4/5, and BF.7 variants. (A) FEL contour plot for BA.1, (B) FEL contour plot for BA.4/5, and (C) FEL contour plot for BF.7. The 3D-contour plots depict the Gibbs FELs obtained from the equilibrated and stable time frames of the MD simulation trajectories, represented as a function of the first two principal components. In the FEL plots, the color scheme represents the energy states: red indicates the high-energy state, yellow and green correspond to the low-energy states, while blue and purple represent the stable states with the lowest energies.

MMPBSA command was executed for the last 30 ns of the trajectories to obtain the output results, which included information about the contributions of various types of energies to the total energies of the receptor, ligand, and the binding free energy of the receptor–ligand complex in each frame as well as the average of all frames. The energetic contributions for the complex, receptor, and ligand are divided into GGAS and GSOLV, where GGAS is the interaction energy and is obtained after summing the internal(bonded) components (BOND + ANGLE + DIHED) and the nonbonded (VDWAALS + EEL) components. For GSOLV, the polar and nonpolar contributions are EGB (or EPB) and ESURF (or ENPOLAR + EDISPER), respectively, for GB (or PB) calculations.

2.5. Contact Analysis. The intermolecular interactions between the RBD and ACE2 were analyzed from the equilibrated and stable time frames of the MD simulation trajectories using GetContacts.[33] The Arpeggio[34] and PIMA[35] web servers were used to calculate the intramolecular interactions and interaction energy at specific snapshots within the RBD-ACE2 complex, respectively. Hydrogen bond interactions were computed using the hydrogen bonds modules of VMD.[36] The hydrogen bonds were also visualized in the PyMOL 2.3.0 Open-Source package,[37] and figures were created using the Matplotlib[38] and Seaborn[39] libraries of Python.

3. RESULTS AND DISCUSSION

3.1. Validation of Modeled Structures of the Variants. The cryo-EM structure solved at 2.66 Å for the BA.1 variant served as the control for validation of the two generated structures, BA.4/5 and BF.7. The stereochemical quality of the structures was evaluated using the PROCHECK module of the SAVES server, which assessed the residue-by-residue geometry. The BA.1 structure was found to have 92.0% of its residues in the most favored regions, which is considered a high-quality structure with a cutoff of 90% or more residues in the most favored regions. This was comparable to the BA.4/5 and BF.7 structures, which also had 92.1% of their residues located in the most favored regions (Figure S1). Furthermore, the ERRAT module of the SAVES server was used to evaluate the statistics of nonbonded interactions between different atoms. The BA.1 structure had 3 residues that surpassed the 95% error limit, while the BA.4/5 and BF.7 structures each had only 1

Table 2. Decomposition of Energies and the Overall End-State Binding Free Energy for the BA.1 Variant from Equilibrated and Stable MD Simulations (All Values Are Reported in kcal/mol)

energy component	average	SD (prop.)[a]	SD[b]	SEM (prop.)[c]	SEM[d]
ΔBOND	0.40	17.19	0.71	2.41	0.10
ΔANGLE	1.28	19.89	1.02	2.79	0.14
ΔDIHED	1.62	12.81	0.40	1.79	0.06
ΔUB	0.00	4.26	0.00	0.60	0.00
ΔIMP	0.41	5.11	0.44	0.72	0.06
ΔCMAP	−0.27	6.33	0.69	0.89	0.10
ΔVDWAALS	−353.88	8.65	8.65	1.21	1.21
ΔEEL	−347.88	32.10	44.13	4.49	6.18
Δ1−4 VDW	1.48	6.95	0.65	0.97	0.09
Δ1−4 EEL	42.49	21.14	1.36	2.96	0.19
ΔEGB	429.76	27.64	37.87	3.87	5.3
ΔESURF	−51.2	0.61	0.7	0.09	0.1
ΔGGAS	−701.61	34.49	42.58	4.83	5.96
ΔGSOLV	378.56	27.65	37.72	3.87	5.28
ΔTOTAL	−323.05	44.20	10.20	6.19	1.43

[a] SD(Prop.)—SD obtained with the propagation of the uncertainty formula. [b] SD—sample standard deviation. [c] SEM(Prop)—SEM obtained with the propagation of the uncertainty formula. [d] SEM—sample standard error of the mean.

Table 3. Decomposition of Energies and Overall End-State Binding Free Energy for the BA.4/5 Variant from Equilibrated and Stable MD Simulations (All Values Are Reported in kcal/mol)

energy component	average	SD (prop.)[a]	SD[bb]	SEM (prop.)[cc]	SEM[dd]
ΔBOND	0.27	16.59	0.32	2.32	0.04
ΔANGLE	1.55	25.44	1.03	3.56	0.14
ΔDIHED	1.65	7.63	0.4	1.07	0.06
ΔUB	0	4.59	0	0.64	0
ΔIMP	0.44	5.79	0.42	0.81	0.06
ΔCMAP	−0.62	5.21	0.55	0.73	0.08
ΔVDWAALS	−345.69	8.92	9.44	1.25	1.32
ΔEEL	−257.15	33.59	56.27	4.7	7.88
Δ1−4 VDW	1.31	11.81	0.47	1.65	0.07
Δ1−4 EEL	42.54	23.57	1.1	3.3	0.15
ΔEGB	345.91	22.44	49.2	3.14	6.89
ΔESURF	−48.59	0.68	0.9	0.1	0.13
ΔGGAS	−603.01	35.91	52.92	5.03	7.41
ΔGSOLV	297.31	22.45	48.9	3.14	6.85
ΔTOTAL	−305.7	42.35	9.46	5.93	1.32

[a] SD(Prop.)—SD obtained with the propagation of the uncertainty formula. [b] SD—sample standard deviation. [c] SEM(Prop)—SEM obtained with the propagation of the uncertainty formula. [d] SEM—sample standard error of the mean.

Table 4. Decomposition of Energies and Overall End-State Binding Free Energy for the BF.7 Variant from Equilibrated and Stable MD Simulations (All Values Are Reported in kcal/mol)

energy component	average	SD (prop.)[a]	SD[b]	SEM (prop.)[cc]	SEM[d]
ΔBOND	0.31	14.82	0.36	4.69	0.11
ΔANGLE	1.29	27.7	0.81	8.76	0.26
ΔDIHED	1.75	9.92	0.43	3.14	0.14
ΔUB	0	3.87	0	1.22	0
ΔIMP	0.39	7.2	0.23	2.28	0.07
ΔCMAP	0.04	3.08	0.64	0.97	0.2
ΔVDWAALS	−363.29	9.37	6.89	2.96	2.18
ΔEEL	−138.58	51.65	43.11	16.33	13.63
Δ1−4 VDW	1.19	8.68	0.4	2.74	0.13
Δ1−4 EEL	42.42	8.85	0.91	2.8	0.29
ΔEGB	253.65	49.09	41.46	15.52	13.11
ΔESURF	−50.77	0.42	1.16	0.13	0.37
ΔGGAS	−501.44	53.22	44.27	16.83	14
ΔGSOLV	202.87	49.09	40.79	15.52	12.9
ΔTOTAL	−298.57	72.4	6.01	22.89	1.9

[a] SD(Prop.)—SD obtained with the propagation of the uncertainty formula. [b] SD—sample standard deviation. [c] SEM(Prop)—SEM obtained with the propagation of uncertainty formula. [d] SEM—sample standard error of the mean.

residue exceeding the limit (Figure S2). The quality factors for BA.1, BA.4/5, and BF.7 were 87.94, 88.33, and 88.59, respectively. These results provide a strong indication of the stability and accuracy of the proposed model.

3.2. Stability, Compactness, and Structural Flexibility of the RBD-ACE2 Complex. The MD simulations were carried out in triplicate for 100 ns for the three systems (BA.1, BA.4/5, and BF.7) to highlight critical structural and conformational differences between the variants of SARS-CoV-2 (Table 1). The structural stability profiles demonstrated similar RMSD profiles for the backbone atoms of the RBD-ACE2 complex for all of the variants over time (Figure 2A). The average RMSD values for all three systems ranged from 0.22 to 0.24 nm (Table S1). Strictly, from the replicated simulations of all of the variants, BA.4/5 experienced marginally higher RMSD for the backbone atoms of the RBD-ACE2 complex (Figure S3 and Table S1). However, within the initial 60−70 ns of the simulation duration, all three systems attain stable states, implying that the trajectory of the last 30−40 ns was the most favorable for structural and dynamic analyses. The average RMSD from the three runs showed nearly similar profiles with very minute deviation and stable values, further indicating the reliability of our simulations (Table S1). Therefore, we utilized the simulations from the first run for subsequent analysis of structural−dynamic−energetic features. Next, the R_g values were calculated from three independent simulations to assess the compactness of the three systems during the simulations (Figures 2B and S4). Similar to the RMSD profiles, the R_g profiles attain a steady range during the first 60−70 ns of the simulations. The average R_g values for all three systems ranged from 3.18 to 3.20 nm (Table S1). Although slight differences in R_g values were observed across the three simulation runs for the three different variants (Figure S4 and Table S1), it was not sufficient to draw a conclusion to highlight which variant indeed exhibits highly compact dynamics of the RBD-ACE2 complex during the simulations. This encouraged us to perform more rigorous quantitative analyses to reflect upon the structural, dynamic, and binding changes of the three variants subsequently. Next, the structural flexibilities of the RBD-ACE2 complex were evaluated by computing the per-residue RMSF (Figure 2C,D). While the RMSF values for the ACE2 receptor were consistent across all three systems, there were evident variations for the RBD. In comparison to the RBD residues of the other systems, the RMSF values for the BA.1 RBD were consistently lower. The average RMSF values

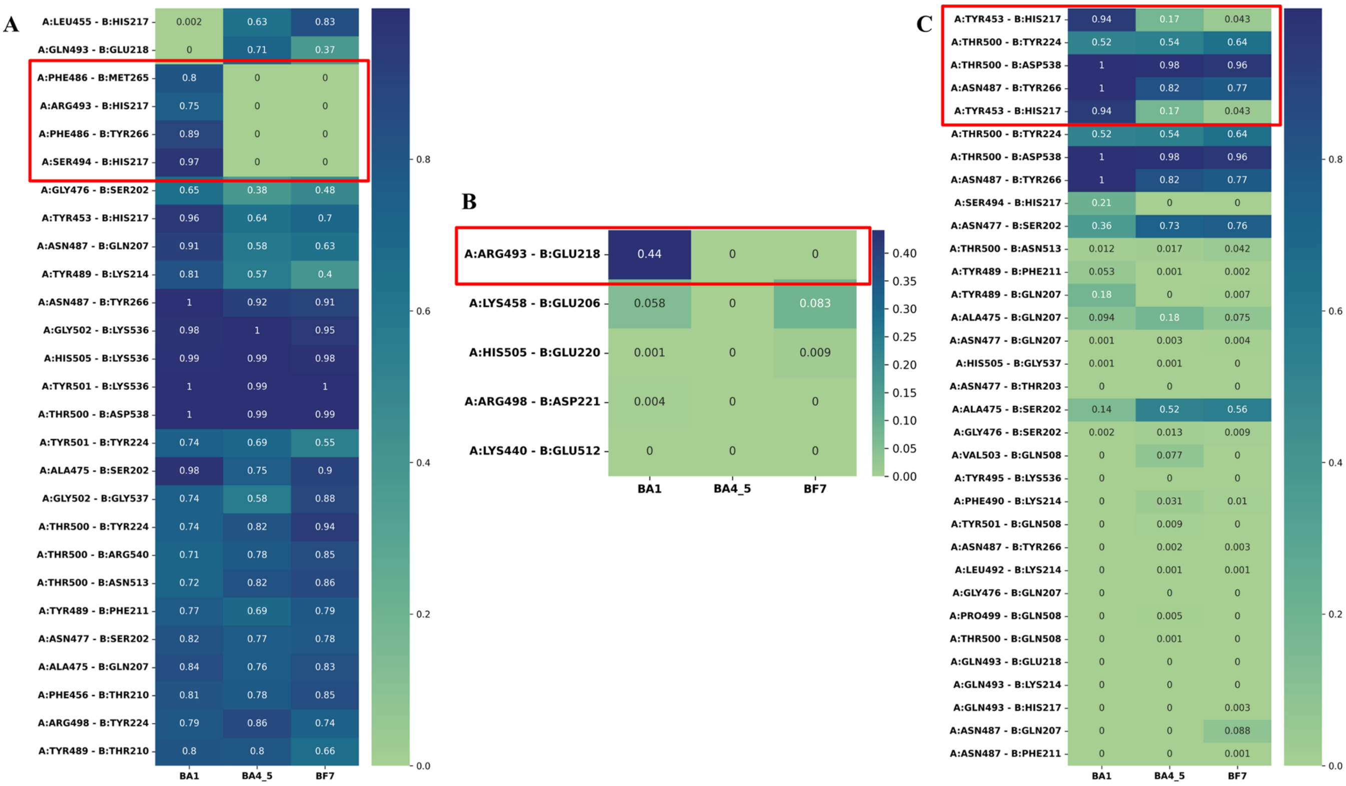

Figure 4. Interactions in RBD-ACE2 complexes of BA.1, BA.4/5, and BF.7 variants. (A) Computed van der Waals interactions, (B) salt bridges, and (C) hydrogen bond interactions for BA.1, BA.4/5, and BF.7 RBD-ACE2 complexes from the equilibrated and stable time frames of the MD simulation trajectories. The gradient of green and blue shades represents the frequency of interactions observed during the 100 ns MD simulation. Cluster grams are used to visualize the contacts for easier interpretation. In the cluster grams, 'A' corresponds to chain A, which represents the RBD of SARS-CoV-2, while 'B' represents chain B, representing the human ACE2 receptor. Interactions predominantly observed in the BA.1 variant compared to the BA.4/5 and BF.7 variants are highlighted within red squares.

for the RBD of all three systems ranged from 0.15 to 0.17 nm. Overall, the RMSD, R_g, and RMSF data showed that BA.1 generates a more stable RBD-ACE2 complex than the other systems. To support this, the detailed dynamics of the three systems was subsequently quantified.

3.3. Principal Component and Free Energy Analyses of the RBD-ACE2 Complex.

PCA is a fundamental method for understanding the correlation of collective atomic motion in the RBD-ACE2 complex of various systems. The eigenvector with the largest associated eigenvalues, which covers most of the system dynamics, was obtained to determine the fundamental subspace of dynamics. For this purpose, stable PCA clusters for BA.1, BA.4/5, and BF.7 were obtained for the backbone atoms of the RBD-ACE2 complex from the equilibrated and stable time frames of the trajectories (Figure S5). Additionally, it establishes the compactness of BA.1 because the trace values of BA.1, BA.4/5, and BF.7's covariance matrices were found to be 29.42, 37.72, and 38.56 nm^2, respectively. The relative contributions of the different eigenvectors to the overall motion show that the first two eigenvectors make up most of the system dynamics, making them better suited for providing structural and correlational insights. According to the Gibbs free energy landscapes (FEL) generated using the PC1 and PC2 (Figure 3), BA.1 has more stable and compact confirmations than BA.4/5 and BF.7 (a more significant number of deep blue energy grooves; here, purple and blue indicate low-energy states, whereas red stands for high-energy states). This is also consistent with earlier observations that all three systems exhibit distinct structural and dynamical behaviors along the trajectory.

3.4. Binding Free Energy of the RBD-ACE2 Complexes of the Variants.

To investigate how strongly the RBD and ACE2 bind to each other in the MD simulation trajectories of the variants and how each energetic term contributed to the binding, the end-state binding free energies were computed using the MMPBSA method. To this end, the last 30 ns of the MD simulation trajectories was investigated to obtain the binding affinities and insights into the binding mechanisms between RBD and ACE2 of the variants. It was found that the BA.1 variant exhibited the high binding free energy of −323.05 kcal/mol among all variants (Table 2). In contrast, the BA.4/5 and BF.7 variants exhibited binding free energies of −305.70 and −298.57 kcal/mol, respectively (Tables 3 and 4). A closer look at the decomposed energetic contributions further revealed that ΔVDWAALS, Δ*E*EL, Δ*E*GB, Δ*G*GAS, and ΔSOLV were the major contributors in determining the binding free energies of the complex (Tables 2−4). Further, the binding energies of the complexes indicating the stability of the variants over the simulations revealed that BA.1 and BF.7 variants exhibited total energies of −10246.10 and −10267.84 kcal/mol compared to −9943.40 kcal/mol in the BA.4/5 variant (Tables S2−S4). Overall, these results demonstrated the higher binding free energy and stability of the BA.1 variant compared to BA.4/5 and BF.7 variants.

3.5. Contact Analyses between RBD and ACE2.

Intermolecular contact analyses between RBD (chain A) and

Table 5. Total Stabilizing Energy and Interactions between RBD and ACE2 Computed Using PIMA

	total stabilizing energy (kJ/mol)			hydrogen bond energy (kJ/mol)			electrostatic energy (kJ/mol)			van der Waals energy (kJ/mol)			number of interface residues			no. of salt bridges			no. of hydrophobic interactions		
time (ns)	BA.1	BA.4/5	BF.7	BA.1	BA.4/5	BF.7	BA.1	BA .4/5	BF.7	BA.1	BA.4/5	BF.7	BA.1	BA .4/5	BF.7	BA.1	BA .4/5	BF.7	BA.1	BA .4/5	BF.7
70	−330.44	−206.63	−257.70	−41.82	−28.36	−55.15	−29.5	6.05	−4.99	−259.07	−184.32	−197.57	95	91	89	1	0	0	2	0	0
80	−245.90	−230.09	−230.18	−25.17	−34.17	−36.00	−5.54	4.03	−3.77	−215.18	−199.96	−190.40	80	93	89	0	0	0	0	1	0
90	−229.79	−231.70	−224.98	−25.08	−35.59	−31.62	−6.72	1.61	−6.76	−197.99	−197.73	−186.54	90	91	87	0	0	0	1	1	2
100	−270.40	−202.99	−204.88	−37.84	−16.56	−19.90	−8.24	3.35	−6.93	−224.31	−189.77	−178.04	94	87	86	0	0	0	1	1	1

Table 6. Total Stabilizing Energy and Interactions between RBD and ACE2 Computed Using Arpeggio

	mutually exclusive contacts			polar contacts						feature contacts														
	VDW interaction			polar contacts			weak polar contacts			hydrogen bonds			weak hydrogen bonds			Ionic interactions			aromatic contacts			hydrophobic contacts		
time (ns)	BA.1	BA.4/5	BF.7	BA.1	BA.4/5	BF.7	BA.1	BA.4/5	BF.7	BA.1	BA.4/5	BF.7	BA.1	BA.4/5	BF.7	BA.1	BA.4/5	BF.7	BA.1	BA.4/5	BF.7	BA.1	BA.4/5	BF.7
70	10	8	9	26	22	22	15	8	15	18	15	15	12	9	9	4	5	4	6	3	1	29	23	21
80	12	14	9	22	23	23	11	15	10	14	14	14	6	10	5	2	3	4	6	5	0	41	21	15
90	12	11	9	21	21	21	10	14	12	13	10	18	13	8	9	5	4	4	3	5	1	26	27	28
100	8	11	10	18	25	20	11	10	11	14	16	14	7	9	8	1	3	2	7	4	4	37	31	27

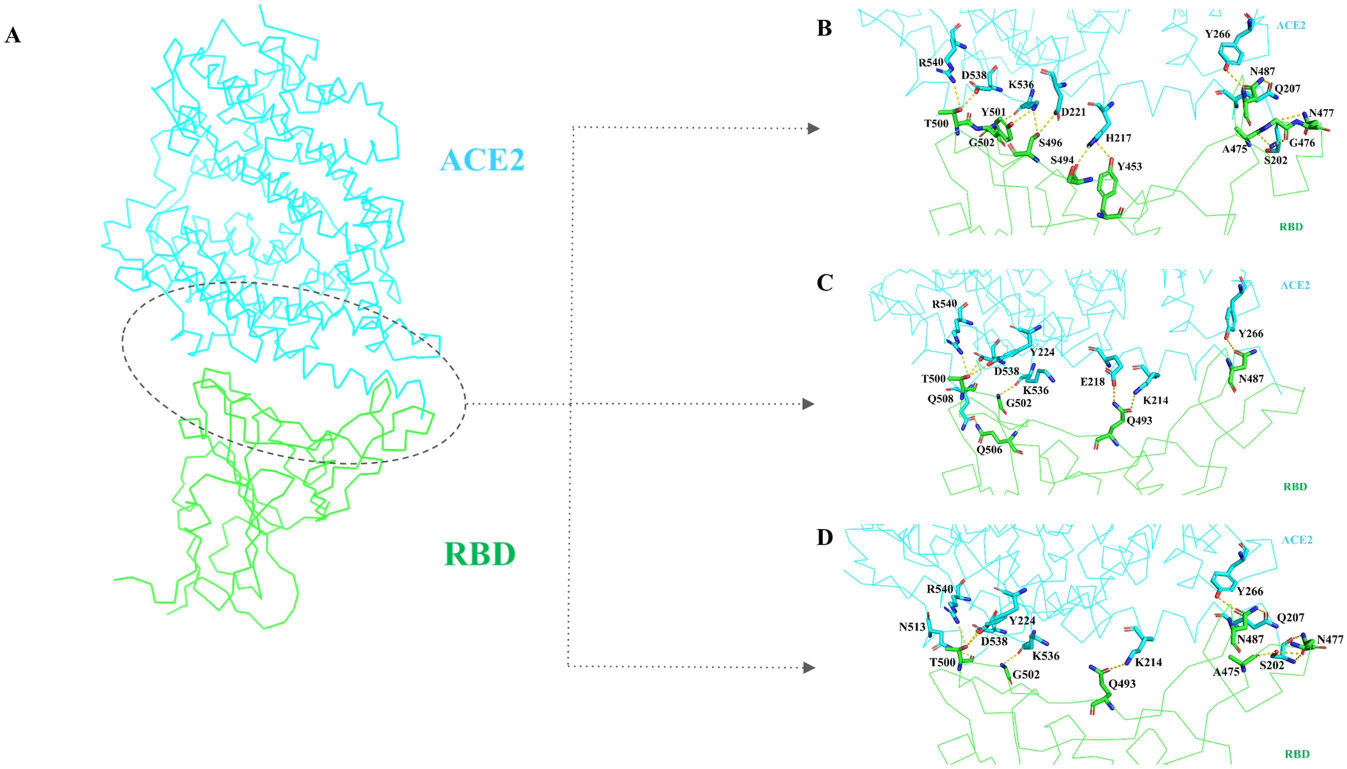

Figure 5. Crucial hydrogen bond interactions in the RBD-ACE2 complex of BA.1, BA.4/5, and BF.7 variants. (A) Overall RBD-ACE2 complex structure with encircled interface residues involved in hydrogen bond interactions with ACE2 in (B) BA.1, (C) BA.4/5, and (D) BF.7 at 70 ns of the simulations, representing the time point where the complex exhibits the maximum difference in overall stabilizing energy. In the figure, 'A' corresponds to chain A, representing the RBD of SARS-CoV-2, while 'B' corresponds to chain B, representing the human ACE2 receptor. The encircled residues highlight the crucial hydrogen bond interactions (shown in yellow dotted lines) between RBD and ACE2 in each variant, providing insights into the specific binding characteristics of BA.1, BA.4/5, and BF.7 variants.

Table 7. RMSD Comparison between Modeled BA.4/5 and Cryo-EM Structure during a 10 ns Time Interval

time (ns)	RMSD (in Å)
0	0.94
10	2.29
20	1.56
30	1.85
40	1.54
50	1.91
60	2.07
70	1.80
80	2.19
90	1.96
100	1.92

ACE2 (chain B) were performed to understand the impact of the mutations on the contact and binding modes. First, for all three systems, we generated various contact maps (Figure 4) representing the occupancy of every van der Waals interaction, salt bridge, and hydrogen bond on a scale of 0−1 throughout the trajectory. As shown in Figure 4A, BA.1 predominates in 25 out of the 27 van der Waals interactions detected by GetContacts. Specifically, BA4.4/5 and BF.7 variants have impaired van der Waals interactions between the interface residues: A:PHE486−B:MET265, A:ARG493−B:HIS217, A:PHE486−B:TYR266, and A:SER494−B:HIS217 (Figure 4A). According to Figure 4B, BA.1 is prominent on an interchain salt bridge (with occupancies ≥40%) between residues: A:ARG493−B:GLU218. Lastly, Figure 4C suggests that BA.1 has an enhanced interaction frequency for the following crucial residues: A:TYR453−B:HIS217, A:ASN487−B:TYR266, A:TYR453−B:HIS217, and A:ASN487−B:TYR266. Here, 'A' denotes chain A, i.e., RBD of SARS-CoV-2, and 'B' denotes chain B, i.e., human ACE2 receptor. Overall, BA.1 dominates in hydrogen bond interactions over BA.4/5 and BF.7 variants (Figure 4C). This is further corroborated by the statistics provided in Tables 5 and 6, which describe the interchain interaction in the snapshots taken over the last 30 ns. In two out of the four frames, BA.1 dominates compared to BA.4/5 and BF.7 in terms of the number of hydrogen bonds and van der Waals interactions.

Additionally, BA.1 has a higher total stabilizing energy in snapshots taken within the last 30 ns (Tables 5 and 6), with van der Waals energy and electrostatic energy accounting for the majority of the energetics. This is consistent with the earlier observations from BA.1, generating a more stable and compact complex. Taking into account the total stabilizing energy, we investigated the interchain hydrogen bond interaction in the snapshot with the largest difference of energy between the systems. The snapshot at 70 ns was taken in order to examine the interchain hydrogen bonds (Figure 5) between RBD and ACE2. In line with earlier discussions, the BA.1 variant displayed 8 unique hydrogen bond interactions (Figure 5A; A:Y453−B:H217, A:A475−B:S202, A:G476−B:S202, A:N477−B:S202, A:N487−B:Q207, A:S494−B:H217, A:S496−B:D221, A:Y501−B:K536), compared to 4 in BA.4/5 (Figure 5B; A:Q493−B:K214, A:Q493−B:E218, A:T500−B:Y224, A:Q506−B:Q508) and 6 in BF.7 (Figure

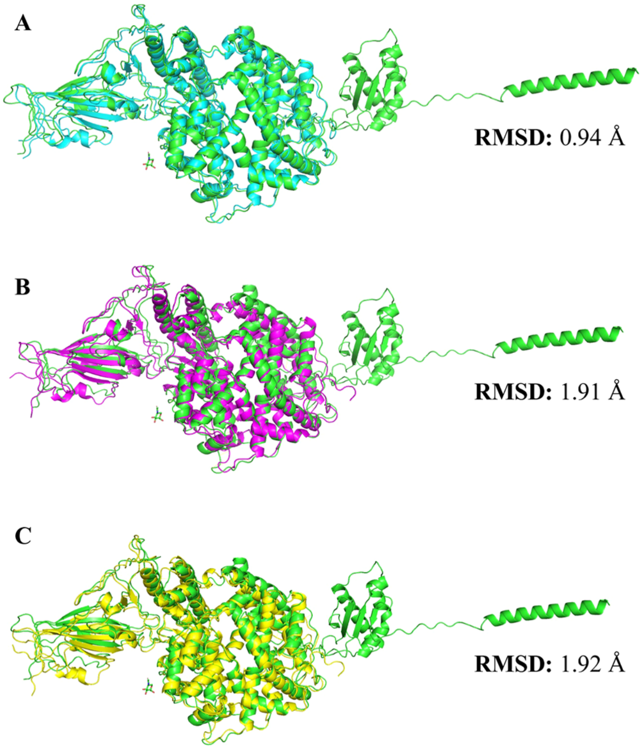

Figure 6. Superimposed structures of the BA.4/5 Variant. Superimposed structure of the BA.4/5 variant at (A) 0 ns and (B) 50 ns, as well as (C) 100 ns of the MD simulation, with the cryo-EM structure of BA.4/5 (PDB ID: 7Y76). The low RMSD observed upon superposition validates the accuracy of our simulations and the fidelity of the resulting snapshots.

5C; A:A475−B:S202, A:N477−B:S202, A:N487−B:Q207, A:Q493−B:K214, A:T500−B:Y224, A:T500−B:N513). Here, 'A' denotes chain A, i.e., RBD of SARS-CoV-2, and 'B' denotes chain B, i.e., human ACE2 receptor. The formation of hydrogen bonds at the 164th position of RBD is not observed in BA.1; however, following the R164Q mutation, hydrogen bonds are formed at the position in BA.4/5 and BF.7.

3.6. Correlation of Computational Results with Reported Structural Data. The structure of BA.4/5 was not available in the Protein Data Bank at the commencement of this investigation. As a result, we mutated specific residues in BA.1 to obtain BA.4/5, as mentioned in Section 2.1. However, during the course of our simulations, the structure of BA.4/5 was made available in the Protein Data Bank (PDB ID: 7Y76). We utilized this structure to check the consistency of the simulation results. In order to examine structural similarity, we computed the RMSD between several snapshots obtained from our simulations and that of the cryo-EM structure of BA.4/5. Specifically, superposition at three different snapshots, taken at 0 ns (Figure 6A), 50 ns (Figure 6B), and 100 ns (Figure 6C), demonstrated the closeness of the conformations between our simulations and the structural information (Figure 6). The reliability of our simulations is supported by the low values of RMSD in each of the three situations (0.94, 1.91, and 1.92 Å), respectively. Table 7 provides the RMSD values of the superimposition of simulated structures captured in a time interval of 10 ns with the cryo-EM structure.

3.7. Correlation of Computational Results with the Variant Prevalence Data. Next, the prevalence data for all of the variants was obtained from outbreak.info (https://outbreak.info/), a reputable source for COVID-19 variant information. The prevalence data of the SARS-CoV-2 variants until early 2023 highlights the dominance of BA.1. The BA.1 (Figure 7A) variant is discernible as the dominant form, accounting for more than 80% of the population of all of the propagating SARS-CoV-2 variants and continuing to increase. However, BA.4/5 (Figure 7B) has a prevalence rate of only 60% as opposed to the maximum 8% in BF.7 (Figure 7C), which is beginning to decline. It is important to note here that the prevalence data does not represent the sum of all of the variants equating to 100%. Rather, the prevalence data presented in our study is reflected on an individual basis for each variant. Further, the calculation of prevalence for a specific variant follows a standard formula, i.e., the number of cases detected for that particular variant divided by the total number of samples sequenced on a given day. This methodology allows for an estimation of the relative proportion of a specific variant within the samples sequenced. Importantly, BA.1 is the most prevalent sublineage, has been detected in the majority of countries across the globe, and is responsible for 99% of cases in the United States. The US CDC has reported that the BF.7 variant accounts for 4.6% of active coronavirus cases in the United States and is currently the third most common variant behind BA.5 and BA.4/5. Most crucially, as of February 2021, 91 countries had a variant with the genetic makeup and mutation profile of BF.7, although its prevalence remained less than 0.5% globally. However, the recent rise of BF.7 cases in China may be attributed to the country's highly vulnerable population to its ineffective vaccine, low rates of vaccination, and poor investment in emergency care. Altogether, the above results indicate that BA.1 exhibited a more stable, compact, and tight complex between RBD and ACE2 than the other variants. This is also supported by the prevalence data, which strengthens the consistency of our MD simulation results and related quantitative analyses, emphasizing the superior fitness of the BA.1 variant over the BA.4/5 and BF.7 variants.

3.8. Limitations of the Study. This study has a few limitations that warrant attention. First, while classical MD simulations undoubtedly provide valuable insights into molecular behavior, they encounter challenges when applied to intricate systems like protein−protein interaction complexes. The complexity of these interactions and the extensive conformational landscape often impede the attainment of sufficient sampling of the potential energy surface (PES) within the confines of typical MD time scales (Figures 2 and 3). This insufficiency in sampling could potentially curtail our grasp of complex stability and dynamics, as evidenced by the identification of local energy minima and barriers across the three variants under study (Figure 3), possibly restricting broader conformational exploration. To address this, we executed simulations in triplicate, each initiated with distinct initial velocities. Furthermore, we are actively engaged in the exploration of multiple independent runs utilizing accelerated sampling methods such as enhanced sampling or replica exchange. Additionally, we have plans to implement coarse-grained molecular dynamics (CG-MD) simulations, which involve employing simplified particle representations to explore larger time scales, facilitating comprehensive insights into complex stability. Second, our study concentrated on the comparative analysis of the BA.1, BA.4/5, and BF.7 variants, which has yielded substantial evidence concerning the stability and binding of the BA.1 variant. However, we acknowledge

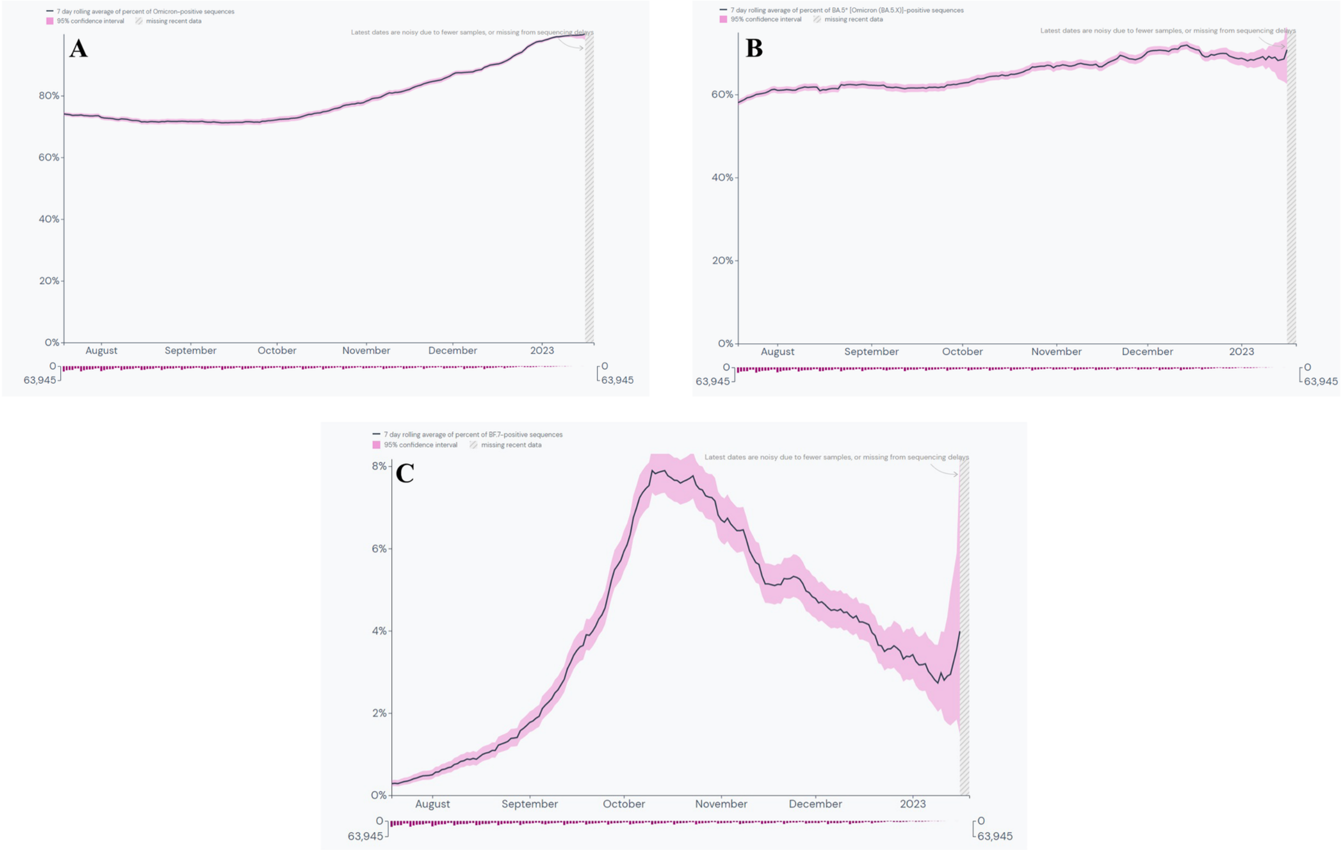

Figure 7. Global prevalence of SARS-CoV-2 variants. Average daily prevalence of (A) BA.1, (B) BA.4/5, and (C) BF.7 variants over the past six months. The prevalence data presented here is obtained from outbreak.info, facilitated by GISAID. It is important to note that the prevalence data does not represent the cumulative sum of all variants equal to 100%. Rather, the prevalence data is specific to each variant individually. The calculation of prevalence for a variant is based on the number of cases detected for that variant divided by the total number of samples sequenced on a given day.

that conclusive evidence regarding the superiority and prevalence of BA.4/5 and BF.7 variants relative to each other is lacking. To comprehensively assess these variants, it is imperative to encompass a broader range of variants considering the prevalence, binding, and experimental details. We are cognizant of the need for further exploration to fully understand the complexities of the interactions between these variants and their potential implications for disease pathophysiology.

4. CONCLUSIONS

In December 2022, a notable surge in the number of COVID-19 cases occurred in multiple countries, particularly China, attributed to the emergence of the BF.7 subvariant of the SARS-CoV-2 omicron variant. This sudden rise of BF.7 necessitated an investigation into its infectivity and virulence in comparison to the highly transmissible and concerning BA.1 variant, also known as the omicron variant. In light of this observation, our study aimed to conduct a comprehensive comparative analysis of the BF.7 variant alongside two other variants, BA.1 and BA.4/5, based on available structural and sequence data, in order to explore their structural, dynamic, and binding properties. To achieve this, we utilized mutagenesis information and the BA.1 crystal structure as a reference to generate high-quality structural models of BA.4/5 and BF.7, which were subsequently validated extensively. The comparative analysis encompassed structural, dynamic, and energetic evaluations based on three replicates of simulations involving BA.1, BA.4/5, and BF.7. Various structural and physicochemical properties, such as RMSD, R_g, RMSF, PCA, and end-state binding free energy calculations, were employed to assess the stability, compactness, and binding characteristics of the RBD-ACE2 complex in each variant.

Our findings consistently indicated that the RBD-ACE2 complex in BA.1 exhibited greater stability, compactness, and stronger binding compared with BA.4/5 and BF.7. This conclusion was supported by analyses of van der Waals contacts and hydrogen bonds, which revealed a higher number of stabilizing interface contacts in BA.1. Furthermore, the calculation of the total stabilizing energy highlighted the dominance of BA.1, particularly during the final 30 ns of the simulation trajectory. The prevalence of BA.1, accounting for 80% of the global spread of the virus over the past six months, further reinforced our study results and underscored the superiority of BA.1 over BA.4/5 and BF.7, which contributed to only 60 and 8.0% of the cases, respectively. The insights obtained from this study are invaluable in understanding the distinct structural, dynamic, and binding attributes of BA.1, BA.4/5, and BF.7 variants. Moreover, these findings have implications for comprehending the molecular mechanisms of other SARS-CoV-2 variants/subvariants and can contribute to the development of targeted therapeutics.[40]

https://doi.org/10.1021/acsomega.3c02904
ACS Omega 2023, 8, 37852−37863

ASSOCIATED CONTENT

Supporting Information

The Supporting Information is available free of charge at https://pubs.acs.org/doi/10.1021/acsomega.3c02904.

> Ramachandran plots for the three systems (Figure S1); analysis of nonbonded interactions in the three systems (Figure S2); comparative RMSD profiles of RBD-ACE2 complex variants (Figure S3); comparative Rg profiles of RBD-ACE2 complex variants (Figure S4); principal component analysis (PCA) clusters of RBD-ACE2 complex variants (Figure S5); average RMSD and Rg values of variants in triplicate replicas (Table S1); detailed decomposition of various energies and overall end-state binding energy of the RBD-ACE2 complexes in BA.1 (Table S2); detailed decomposition of various energies and overall end-state binding energy of the RBD-ACE2 complexes in BA.4/5 (Table S3); and detailed decomposition of various energies and overall end-state binding energy of the RBD-ACE2 complexes in BF.7 (Table S4) (PDF)

AUTHOR INFORMATION

Corresponding Authors

Timir Tripathi − *Molecular and Structural Biophysics Laboratory, Department of Biochemistry, North-Eastern Hill University, Shillong 793022, India;* orcid.org/0000-0001-5559-289X; Email: timir.tripathi@gmail.com

Aditya K. Padhi − *Laboratory for Computational Biology & Biomolecular Design, School of Biochemical Engineering, Indian Institute of Technology (BHU), Varanasi 221005 Uttar Pradesh, India;* orcid.org/0000-0001-6732-2547; Email: aditya.bce@iitbhu.ac.in, dradityapadhi@gmail.com

Authors

Aryaman Joshi − *Department of Chemical Engineering & Technology, Indian Institute of Technology (BHU), Varanasi 221005 Uttar Pradesh, India;* orcid.org/0000-0002-9837-673X

Shweata Maurya − *Laboratory for Computational Biology & Biomolecular Design, School of Biochemical Engineering, Indian Institute of Technology (BHU), Varanasi 221005 Uttar Pradesh, India*

Atharva Mahale − *Department of Biotechnology, National Institute of Technology, Warangal 506004 Telangana, India*

Soumya Lipsa Rath − *Department of Biotechnology, National Institute of Technology, Warangal 506004 Telangana, India;* orcid.org/0000-0003-0767-3016

Complete contact information is available at: https://pubs.acs.org/10.1021/acsomega.3c02904

Notes

The authors declare no competing financial interest.

ACKNOWLEDGMENTS

The authors sincerely acknowledge the infrastructure facilities of IIT (BHU) Varanasi and DST-funded I-DAPT Hub Foundation, IIT (BHU) [DST/NMICPS/TIH11/IIT(BHU) 2020/02]. Further, the computing resources of PARAM Shivay Facility under the National Supercomputing Mission, Government of India at the IIT (BHU), Varanasi, are gratefully acknowledged. S.M. acknowledges Ministry of Human Resource Development (MHRD), Government of India and IIT (BHU) for her fellowship. T.T. acknowledges the support of a project grant from the Indian Council of Medical Research (ICMR) (Grant 52/06/2020/BIO/BMS) Government of India, India. A.K.P. is grateful for the financial support received from the Indian Institute of Technology (Banaras Hindu University) Varanasi's Seed Grant Ref No. IIT (BHU)/Budget/19-(14)/2022-23/17507.

REFERENCES

(1) Rath, S. L.; Padhi, A. K.; Mandal, N. Scanning the RBD-ACE2 molecular interactions in Omicron variant. *Biochem. Biophys. Res. Commun.* **2022**, *592*, 18−23. From NLM Medline.

(2) Wu, C. R.; Yin, W. C.; Jiang, Y.; Xu, H. E. Structure genomics of SARS-CoV-2 and its Omicron variant: drug design templates for COVID-19. *Acta Pharmacol. Sin.* **2022**, *43* (12), 3021−3033. From NLM Medline.

(3) Chan, J. F.-W.; Kok, K. H.; Zhu, Z.; Chu, H.; To, K. K.; Yuan, S.; Yuen, K. Y. Genomic characterization of the 2019 novel human-pathogenic coronavirus isolated from a patient with atypical pneumonia after visiting Wuhan. *Emerging Microbes Infect.* **2020**, *9* (1), 221−236. From NLM Medline.

(4) Harvey, W. T.; Carabelli, A. M.; Jackson, B.; Gupta, R. K.; Thomson, E. C.; Harrison, E. M.; Ludden, C.; Reeve, R.; Rambaut, A.; Peacock, S. J.; Consortium, C.-G. U. SARS-CoV-2 variants, spike mutations and immune escape. *Nat. Rev. Microbiol.* **2021**, *19* (7), 409−424. From NLM Medline.

(5) Wu, L.; Zhou, L.; Mo, M.; Liu, T.; Wu, C.; Gong, C.; Lu, K.; Gong, L.; Zhu, W.; Xu, Z. SARS-CoV-2 Omicron RBD shows weaker binding affinity than the currently dominant Delta variant to human ACE2. *Signal Transduct Target Ther.* **2022**, *7* (1), No. 8, DOI: 10.1038/s41392-021-00863-2. From NLM Medline.

(6) Zhai, X.; Sun, J.; Yan, Z.; Zhang, J.; Zhao, J.; Zhao, Z.; Gao, Q.; He, W. T.; Veit, M.; Su, S. Comparison of Severe Acute Respiratory Syndrome Coronavirus 2 Spike Protein Binding to ACE2 Receptors from Human, Pets, Farm Animals, and Putative Intermediate Hosts. *J. Virol.* **2020**, *94* (15), 10−1128, DOI: 10.1128/JVI.00831-20.

(7) Qu, P.; Evans, J. P.; Faraone, J. N.; Zheng, Y. M.; Carlin, C.; Anghelina, M.; Stevens, P.; Fernandez, S.; Jones, D.; Lozanski, G.; et al. Enhanced neutralization resistance of SARS-CoV-2 Omicron subvariants BQ.1, BQ.1.1, BA.4.6, BF.7, and BA.2.75.2. *Cell Host Microbe* **2023**, *31* (1), 9−17 e13. From NLM Medline.

(8) Padhi, A. K.; Tripathi, T. Can SARS-CoV-2 Accumulate Mutations in the S-Protein to Increase Pathogenicity? *ACS Pharmacol. Transl. Sci.* **2020**, *3* (5), 1023−1026.

(9) Evans, J. P.; Zeng, C.; Qu, P.; Faraone, J.; Zheng, Y. M.; Carlin, C.; Bednash, J. S.; Zhou, T.; Lozanski, G.; Mallampalli, R.; et al. Neutralization of SARS-CoV-2 Omicron sub-lineages BA.1, BA.1.1, and BA.2. *Cell Host Microbe* **2022**, *30* (8), 1093−1102 e1093. From NLM Medline.

(10) Kurhade, C.; Zou, J.; Xia, H.; Cai, H.; Yang, Q.; Cutler, M.; Cooper, D.; Muik, A.; Jansen, K. U.; Xie, X.; et al. Neutralization of Omicron BA.1, BA.2, and BA.3 SARS-CoV-2 by 3 doses of BNT162b2 vaccine. *Nat. Commun.* **2022**, *13* (1), No. 3602. From NLM Medline.

(11) Qu, P.; Evans, J. P.; Zheng, Y. M.; Carlin, C.; Saif, L. J.; Oltz, E. M.; Xu, K.; Gumina, R. J.; Liu, S. L. Evasion of Neutralizing Antibody Response by the SARS-CoV-2 BA.2.75 Variant *bioRxiv* 2022 DOI: 10.1101/2022.08.14.503921.

(12) Gangavarapu, K.; Latif, A. A.; Mullen, J. L.; Alkuzweny, M.; Hufbauer, E.; Tsueng, G.; Haag, E.; Zeller, M.; Aceves, C. M.; Zaiets, K.; et al. Outbreak.info genomic reports: scalable and dynamic surveillance of SARS-CoV-2 variants and mutations. *Nat. Methods* **2023**, *20*, 512−522, DOI: 10.21203/rs.3.rs-1723829/v1. From NLM PubMed-not-MEDLINE.

(13) Arora, P.; Zhang, L.; Rocha, C.; Sidarovich, A.; Kempf, A.; Schulz, S.; Cossmann, A.; Manger, B.; Baier, E.; Tampe, B.; et al. Comparable neutralisation evasion of SARS-CoV-2 omicron sub-

variants BA.1, BA.2, and BA.3. *Lancet Infect. Dis.* **2022**, *22* (6), 766−767. From NLM Medline.

(14) Mohapatra, R. K.; Kandi, V.; Sarangi, A. K.; Verma, S.; Tuli, H. S.; Chakraborty, S.; Chakraborty, C.; Dhama, K. The recently emerged BA.4 and BA.5 lineages of Omicron and their global health concerns amid the ongoing wave of COVID-19 pandemic - Correspondence. *Int. J. Surg.* **2022**, *103*, No. 106698. From NLM Medline.

(15) Shrestha, L. B.; Foster, C.; Rawlinson, W.; Tedla, N.; Bull, R. A. Evolution of the SARS-CoV-2 omicron variants BA.1 to BA.5: Implications for immune escape and transmission. *Rev. Med. Virol.* **2022**, *32* (5), No. e2381. From NLM Medline.

(16) Abu-Raddad, L. J.; Chemaitelly, H.; Ayoub, H. H.; AlMukdad, S.; Yassine, H. M.; Al-Khatib, H. A.; Smatti, M. K.; Tang, P.; Hasan, M. R.; Coyle, P.; et al. Effect of mRNA Vaccine Boosters against SARS-CoV-2 Omicron Infection in Qatar. *N. Engl. J. Med.* **2022**, *386* (19), 1804−1816. From NLM Medline.

(17) Gruell, H.; Vanshylla, K.; Tober-Lau, P.; Hillus, D.; Schommers, P.; Lehmann, C.; Kurth, F.; Sander, L. E.; Klein, F. mRNA booster immunization elicits potent neutralizing serum activity against the SARS-CoV-2 Omicron variant. *Nat. Med.* **2022**, *28* (3), 477−480. From NLM Medline.

(18) Cao, Y.; Wang, J.; Jian, F.; Xiao, T.; Song, W.; Yisimayi, A.; Huang, W.; Li, Q.; Wang, P.; An, R.; et al. Omicron escapes the majority of existing SARS-CoV-2 neutralizing antibodies. *Nature* **2022**, *602* (7898), 657−663. From NLM Medline.

(19) Xia, H.; Zou, J.; Kurhade, C.; Cai, H.; Yang, Q.; Cutler, M.; Cooper, D.; Muik, A.; Jansen, K. U.; Xie, X.; et al. Neutralization and durability of 2 or 3 doses of the BNT162b2 vaccine against Omicron SARS-CoV-2. *Cell Host Microbe* **2022**, *30* (4), 485−488 e483. From NLM Medline.

(20) Padhi, A. K.; Rath, S. L.; Tripathi, T. Accelerating COVID-19 Research Using Molecular Dynamics Simulation. *J. Phys. Chem. B* **2021**, *125* (32), 9078−9091. From NLM Medline.

(21) Kumar, S.; Karuppanan, K.; Subramaniam, G. Omicron (BA.1) and sub-variants (BA.1.1, BA.2, and BA.3) of SARS-CoV-2 spike infectivity and pathogenicity: A comparative sequence and structural-based computational assessment. *J. Med. Virol.* **2022**, *94* (10), 4780−4791. From NLM Medline.

(22) Colovos, C.; Yeates, T. O. Verification of protein structures: patterns of nonbonded atomic interactions. *Protein Sci.* **1993**, *2* (9), 1511−1519. From NLM Medline.

(23) Laskowski, R. A.; MacArthur, M. W.; Moss, D. S.; Thornton, J. M. PROCHECK: a program to check the stereochemical quality of protein structures. *J. Appl. Crystallogr.* **1993**, *26*, 283−291.

(24) Laskowski, R. A.; Rullmannn, J. A.; MacArthur, M. W.; Kaptein, R.; Thornton, J. M. AQUA and PROCHECK-NMR: programs for checking the quality of protein structures solved by NMR. *J. Biomol. NMR* **1996**, *8* (4), 477−486. From NLM Medline.

(25) Abraham, M. J.; Murtola, T.; Schulz, R.; Páll, S.; Smith, J.; Hess, B.; Lindahl, E. GROMACS: High performance molecular simulations through multi-level parallelism from laptops to supercomputers. *SoftwareX* **2015**, *1−2*, 19−25, DOI: 10.1016/j.softx.2015.06.001.

(26) Brooks, B. R.; Brooks, C. L., 3rd; Mackerell, A. D., Jr.; Nilsson, L.; Petrella, R. J.; Roux, B.; Won, Y.; Archontis, G.; Bartels, C.; Boresch, S.; et al. CHARMM: the biomolecular simulation program. *J. Comput. Chem.* **2009**, *30* (10), 1545−1614. From NLM Medline.

(27) Lemak, A. S.; Balabaev, N. K. On The Berendsen Thermostat. *Mol. Simul.* **1994**, *13* (3), 177−187.

(28) Martoňák, R.; Laio, A.; Parrinello, M. Predicting crystal structures: the Parrinello-Rahman method revisited. *Phys. Rev. Lett.* **2003**, *90* (7), No. 075503. From NLM PubMed-not-MEDLINE.

(29) Darden, T. A.; York, D. M.; Pedersen, L. G. Particle mesh Ewald: An N·log(N) method for Ewald sums in large systems. *J. Chem. Phys.* **1993**, *98*, 10089−10092.

(30) Hess, B.; Bekker, H.; Berendsen, H.; Fraaije, J. LINCS: A Linear Constraint Solver for molecular simulations. *J. Comput. Chem.* **1998**, *18*, 1463−1472, DOI: 10.1002/(SICI)1096-987X(199709)18:123.0.CO;2-H.

(31) Valdés-Tresanco, M. S.; Valdes-Tresanco, M. E.; Valiente, P. A.; Moreno, E. gmx_MMPBSA: A New Tool to Perform End-State Free Energy Calculations with GROMACS. *J. Chem. Theory Comput.* **2021**, *17* (10), 6281−6291. From NLM PubMed-not-MEDLINE.

(32) Padhi, A. K.; Seal, A.; Khan, J. M.; Ahamed, M.; Tripathi, T. Unraveling the mechanism of Arbidol binding and inhibition of SARS-CoV-2: Insights from atomistic simulations. *Eur. J. Pharmacol.* **2021**, *894*, No. 173836. From NLM Medline.

(33) Venkatakrishnan, A.; Fonseca, R.; Ma, A.; Hollingsworth, S.; Chemparathy, A.; Hilger, D.; Kooistra, A.; Ahmari, R.; Babu, M.; Kobilka, B.et al.Uncovering patterns of atomic interactions in static and dynamic structures of proteins *bioRxiv* 2019 DOI: 10.1101/840694.

(34) Jubb, H. C.; Higueruelo, A. P.; Ochoa-Montano, B.; Pitt, W. R.; Ascher, D. B.; Blundell, T. L. Arpeggio: A Web Server for Calculating and Visualising Interatomic Interactions in Protein Structures. *J. Mol. Biol.* **2017**, *429* (3), 365−371. From NLM Medline.

(35) Mathew, O.; Sowdhamini, R. PIMA: Protein-Protein interactions in Macromolecular Assembly - a web server for its Analysis and Visualization. *Bioinformation* **2016**, *12* (1), 9−11, DOI: 10.6026/97320630012009. From NLM PubMed-not-MEDLINE.

(36) Humphrey, W.; Dalke, A.; Schulten, K. VMD: visual molecular dynamics. *J. Mol. Graphics* **1996**, *14* (1), 33−38. 27−38. From NLM Medline.

(37) Lilkova, E.; Petkov, P.; Ilieva, N.; Litov, L. *The PyMOL Molecular Graphics System*, Schrodinger, LLC 2015.

(38) Hunter, J. D. Matplotlib: A 2D Graphics Environment. *Computi. Sci. Eng.* **2007**, *9* (3), 90−95.

(39) Waskom, M. seaborn: statistical data visualization. *J. Open Source Software* **2021**, *6*, No. 3021, DOI: 10.21105/joss.03021.

(40) Kalita, P.; Tripathi, T.; Padhi, A. K. Computational Protein Design for COVID-19 Research and Emerging Therapeutics. *ACS Cent. Sci.* **2023**, *9* (4), 602−613. From NLM PubMed-not-MEDLINE.